PAPER

Shape estimation of a bent and twisted cylinder using strain from a sensor array in triple helices

To cite this article: Sungyeop Lim and Soonhung Han 2018 *Meas. Sci. Technol.* **29** 095003

IOP Publishing Measurement Science and Technology
Meas. Sci. Technol. **29** (2018) 095003 (10pp) https://doi.org/10.1088/1361-6501/aacfb6

Shape estimation of a bent and twisted cylinder using strain from a sensor array in triple helices

Sungyeop Lim[1] **and Soonhung Han**[1,2]

[1] iCAD Laboratory, Dept. of Mechanical Engineering, KAIST

E-mail: shhan@kaist.ac.kr

Received 19 March 2018, revised 12 June 2018
Accepted for publication 28 June 2018
Published 26 July 2018

Abstract

This study proposes the use of strain sensors in a triple-helix configuration to measure the bending and twist deformation in a cylinder. Arranging the strain sensors on the cylinder in a triple-helix structure allows us to measure the twist and bending deformation simultaneously. The method consists of two steps: first to determine the local deformation factors from the surface strains, and second to reconstruct the overall deflected shape of the cylinder from the local deformation factors. We derived an exact analytical formula for the surface strain on a bent and twisted cylinder according to the deformation variables based on our original superhelix model, in which we regard the deformed cylinder segment as a helical coil and the sensors bound upon it as segments of superhelices. The local deflection rates are iteratively computed by the Newton–Raphson method using the surface strain formula. We incorporate the local deflection rates into the helical extension method, which is an exact solution to the Frenet–Serret formulas, to reconstruct the overall deflected shape of the cylinder. From the simulations, the proposed method was shown to determine the overall deformation state of a cylindrical body with remarkable precision. The position errors decreased rapidly with shorter spatial intervals of strain sensing and lower rates of the helical periodicity of the sensor arrays, showing a strong trend of convergence. Moreover, the pin-pointedness of the strain sensing was found to be one of the most crucial factors when attempting to ensure high accuracy of the shape estimation results. This study demonstrates a potential for general applicability to various fields, especially for the shape sensing of multicore optical fibers.

Keywords: shape sensing, deformation geometry, cylinder, helix, Frenet–Serret formulas

(Some figures may appear in colour only in the online journal)

1. Introduction

Estimating the shape of a deforming cylindrical rod from its surface strains has been given a considerable attention since Wilk (1988) [1]. Some recent studies have reported the shape sensing of various deformable cylinder-shaped structures such as pipelines [2], endoscopes [3, 4], biopsy needles [5], robotic surgical instruments [6, 7], and multicore optical fibers [8–12].

Most existing studies on the shape sensing of cylindrical rods focused on optical strain sensing methods, while only a few presented the deformation geometry models or numerical procedures used. Wilk showed several detailed formulations by which to determine the deformation state of a cylindrical rod under bending, twisting, shear, and elongation. However, he did not cover cases in which bending and twisting take place at the same time, as doing so requires a proper geometric model of the strain on the surface of the rod. Recently, Zhang *et al* (2013) [2], Askins *et al* (2008) [8], and Froggatt *et al* (2014) [10] introduced a number of approximate methods for the shape estimation of a bent and twisted rod. Askins modeled the strain caused by the combination of bending and twist as a linear combination, and Froggatt employed the Pythagoras'

[2] Author to whom any correspondence should be addressed.

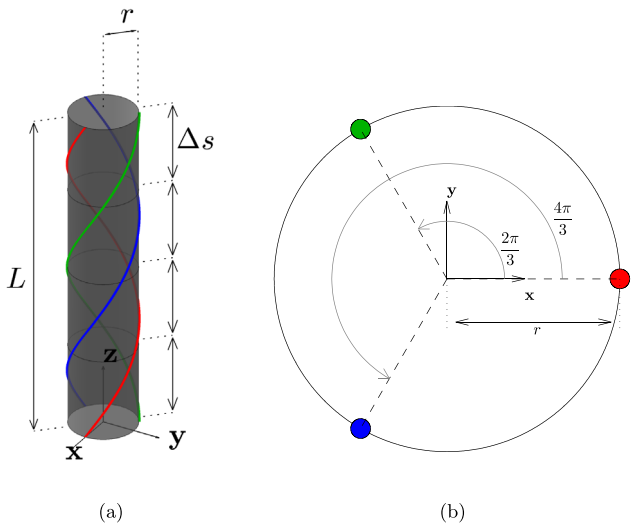

Figure 1. (a) A typical cylinder under test in its undeformed state. In this example, the cylinder is divided into four sampling segments. The three strands of helical fibers are depicted by the red, green, and blue curves. (b) The cross-section at $s = 0$ is represented on the xy plane. In every cross-section, the fibers are arranged to form an equilateral triangle, displaced from the center by radius r and angled apart from one another by 120 degrees.

theorem to decompose the bend-induced strain and the twist-induced strain on the surface. Zhang approximated the strain by modeling the fiber shape as an Archimedean spiral. The effect of Frenet–Serret torsion was neglected in these studies. Froggatt's model proved to be particularly applicable for helically wound multi-core optical fibers, for which the strains can be measured with very high resolutions using Rayleigh scattering. However, the deformation geometries proposed in these reports are not precise descriptions of the three-dimensional (3D) deformation of a rod, but are rather more of a crude approximation.

In our previous works [13, 14], we suggested a curve known as a superhelix to model the geodesics on the curved surface of a bent and twisted cylinder. A superhelix is a 3D space curve that is helically coiled around a helix, which can represent the geodesics on the surface of a cylinder subjected to 3D bending, and hence can be used as a deformation geometry model for the shape sensing of a cylinder. A superhelix is especially effective as a geometric model for strain sensors that are laid in a helical configuration, where the rate of spin of the helix is meant to change according to twist deformation.

In one of our recent studies [15], we introduced the helical extension method (HEM), a new method for reconstructing a 3D space curve from its curvature and torsion, which may be useful for the shape sensing of a rod that is subjected to 3D bending. This method, as the name implies, regards each segment of the curve as a helix, and has been shown to outperform the conventional 4th order Runge–Kutta method.

In this study, we aim to demonstrate the entire numerical procedure of shape sensing, by combining the theories we developed in our two previous works. We will cover in detail how the deformation state of a cylindrical rod is precisely determined from strain measurements from the sensors that are bound on the surface of the rod in triple helices.

Later in this paper, we specify our problem in detail and show how the shape estimation is done in section 2. In section 3, we present a numerical simulation to validate our method and show the results. The conclusion and future works are presented in section 4.

2. Numerical procedure

The triple helix configuration seems to be an ideal sensor formation for measuring the bending and twist of a cylinder. It comprises three arrays of sensors helically wound on the cylinder's surface at a constant rotational rate and with equal angular gaps apart from one another. This formation allows us to measure the twist and bending deformation simultaneously, and fits the number of sensors per segment to its minimum, which is equal to the degree of freedom of bending and twist. It also gets the information of strain measurements radially balanced, and keeps the fiber formation on the cross-sections conserved throughout the length of the fiber.

The cylinder under test is presumed to have three sets of fiber optic strain sensors attached in a triple helix form on its surface. For convenience, hereafter we will refer to these sets of sensors as fibers. Although each of the fiber strands is continuous, the strain measurement is normally done in a discrete fashion. Therefore, there is bound to be a certain basic gauge length depending on the spatial resolution of the strain sensing method being used. In this study, we assume that the cylinder is divided into segments of equal lengths and that the strains are received from three fiber segments for each segment. The cross-sections of the cylinder that border each pair of consecutive segments are called nodes. Figure 1 shows the overall shape of a typical cylinder under test in its undeformed state. The fibers are depicted by the red, green, and blue curves. The 3D positions of the centerline of a cylinder and the sensors that are twined on the surface can be parametrized as

$$\mathbf{C}(s) = \begin{bmatrix} 0 \\ 0 \\ s \end{bmatrix}, \tag{1}$$

and

$$\mathbf{F}(s) = \begin{bmatrix} r\cos(\omega_o s + \theta_i) \\ r\sin(\omega_o s + \theta_i) \\ s \end{bmatrix}, \quad i = 1, 2, 3, \tag{2}$$

respectively, where $0 \leqslant s \leqslant L$ is the arclength parameter of the centerline of the cylinder, and ω_o is the initial rate of spin of the helix with respect to s on the undeformed cylinder. The angle θ_i represents the direction of the fibers at $s = 0$ on the xy plane as shown in figure 1(b). In this study, we let $\theta_1 = 0$, $\theta_2 = \frac{2\pi}{3}$, and $\theta_3 = \frac{4\pi}{3}$.

In this study, we ignore the thickness of the fibers and represent their positions by the center of the cross-section of the fiber in each case. Moreover, we regard the cylindrical surface that includes the fibers' central curves as the surface of our cylinder.

To redefine our problem, we are supposed to determine the following.

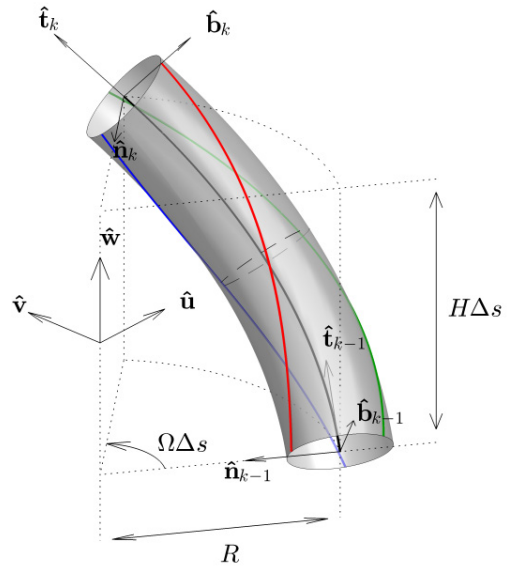

(a)

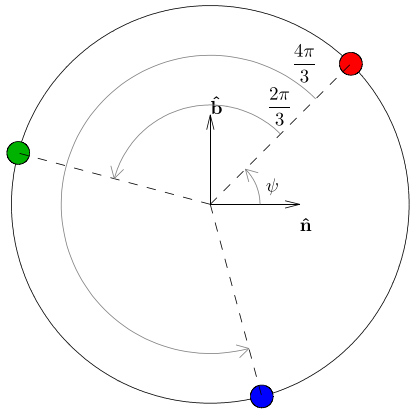

(b)

Figure 2. Modeling of a cylinder segment subjected to bending and twisting at constant rates. (a) The central curve deflects into a helix, and the fibers bound on the surface become superhelices. (b) The fiber phase ψ represents the azimuth angle of the red fiber on the $\hat{\mathbf{n}}\hat{\mathbf{b}}$-plane in the cross-section that halves the segment.

- The local deformation factors of each segment: The curvature of the central curve κ, the torsion of the central curve τ, the azimuth angle of the first fiber from the bending direction in the halfway cross-section of the segment ψ, and the rate at which the fiber is wound on the cylinder ω.
- The overall shape of the deformed cylinder: Central node positions and fiber node positions.

These factors are determined with the following information,

- The cylinder and the fibers in the undeformed state: The overall length of the cylinder L, the radius of the cylinder r, the number of segments N_{seg}, the length of a segment Δs, and the original rate of spin of the fibers ω_o.
- The clamped end ($s = 0$) of the cylinder: The position of the center of the cylinder at $s = 0$, the position of the fibers at $s = 0$, and the tangential direction of the central curve of the cylinder at $s = 0$.
- The strains on the surface received from the sensors after deformation

under the following assumptions.

- The cross-sections are conserved undeformable and perpendicular.
- The cylinder is neither elongated nor compressed along its central axis, and hence the central curve stays unit-speed after deformation.
- The deformation is bending and twisting only.

Our solution to this problem is a two-stage procedure. First, we determine the local deformation factors from the surface strains, after which we reconstruct the overall shape of the cylinder from the local deformation factors by positioning the central and fiber nodes.

2.1. Determining the local deformation factors from the local strains

At this stage, the strains received from the three fiber segments ϵ_1, ϵ_2, and ϵ_3 are used to obtain the local deformation factors, ψ, κ, τ, and ω. ψ represents the direction of the fibers away from the bending direction, and hence indicates the bending direction. κ and τ represent the curvature and the rate of change of the bending direction of the central curve, respectively. ω represents the rate at which the fibers are spun on the cylinder, which changes due to twist deformation of the cylinder, hence indicates the degree of twist.

We determine κ, ψ, and ω first, and then calculate τ from its relation with ψ, and ω. During this process, the fiber segments are assumed to take the form of segments of superhelices, as shown in figure 2. In our previous works [13, 14], we derived the equation of a superhelix, as

$$\mathbf{F}(s) = \begin{pmatrix} \frac{\kappa}{\kappa^2+\tau^2}\cos\left(\sqrt{\kappa^2+\tau^2}s\right) - r\cos\left((\omega-\tau)s+\psi\right)\cos\left(\sqrt{\kappa^2+\tau^2}s\right) \\ \quad +r\frac{\tau}{\sqrt{\kappa^2+\tau^2}}\sin\left((\omega-\tau)s+\psi\right)\sin\left(\sqrt{\kappa^2+\tau^2}s\right) \\ \frac{\kappa}{\kappa^2+\tau^2}\sin\left(\sqrt{\kappa^2+\tau^2}s\right) - r\cos\left((\omega-\tau)s+\psi\right)\sin\left(\sqrt{\kappa^2+\tau^2}s\right) \\ \quad -r\frac{\tau}{\sqrt{\kappa^2+\tau^2}}\sin\left((\omega-\tau)s+\psi\right)\cos\left(\sqrt{\kappa^2+\tau^2}s\right) \\ \frac{\tau}{\sqrt{\kappa^2+\tau^2}}s + r\frac{\kappa}{\sqrt{\kappa^2+\tau^2}}\sin\left((\omega-\tau)s+\psi\right) \end{pmatrix}, \tag{3}$$

by which we can express the shape of the deformed fiber segments as shown in figure 2(a). Here, I used parentheses instead of square brackets to indicate that these coordinates are represented in the local *uvw*-frame, in contrast to (1) and (2) which were written in the global *xyz*-frame. The $\hat{\mathbf{u}}$-axis of the local coordinate is equivalent to the opposite direction of $\hat{\mathbf{n}}$ in figure 2(b), which is the normal vector at the midpoint of the central curve segment, and the $\hat{\mathbf{w}}$-axis is the axis of the central helix. In the local frame, $s = 0$ at the midpoint of the segment, and $-\frac{\Delta_s}{2} \leqslant s \leqslant \frac{\Delta_s}{2}$.

A more detailed derivation of (3) can be found in our previous work [13]. In that study, we attempted to derive an analytical formula for the arc length of a superhelix, which eventually served to determine the strain on a deforming cylinder from the change in the length of an infinitesimal section along the curve on the cylinder's surface. However, it was found that it was not simple to derive a complete and concise formula for the arc length of a superhelix; hence there remains no exact method with which to assess the strain on the surface of a deforming cylinder.

Recently, we found an alternative means of formulating the strain on the surface of a cylinder, once again by using the superhelix model. In this new method, we employ the rate of spatial progression, instead of the arc length, of a superhelix. By letting $\mathbf{F}(s) = [F_1(s)\ F_2(s)\ F_3(s)]^{\mathsf{T}}$, we can express the rate of spatial progression of a superhelix as

$$\begin{aligned} v(s) &= \sqrt{\left[\frac{\mathrm{d}}{\mathrm{d}s}F_1(s)\right]^2 + \left[\frac{\mathrm{d}}{\mathrm{d}s}F_2(s)\right]^2 + \left[\frac{\mathrm{d}}{\mathrm{d}s}F_3(s)\right]^2} \\ &= \sqrt{[1 - r\kappa\cos((\omega-\tau)s + \psi)]^2 + (r\omega)^2}. \end{aligned} \tag{4}$$

Since $v(s)$ is the rate with respect to s, the arc length of a superhelix can be obtained by integrating $v(s)$ over s. From the definition of the nominal strain, we have the strain on the cylinder's surface within the section $[s, s+\delta s]$ as

$$\begin{aligned} \epsilon &= \frac{l - l_o}{l_o} \\ &= \frac{\int_s^{s+\delta s} v(\sigma)\mathrm{d}s}{\int_s^{s+\delta s} v_o(\sigma)\mathrm{d}s} - 1, \end{aligned} \tag{5}$$

where l_o and v_o represent the undeformed length and the undeformed spatial progression rate, respectively. By making δs approach zero, we can have the strain parameterized with s as

$$\begin{aligned} \epsilon(s) &= \lim_{\delta s\to 0} \frac{\int_s^{s+\delta s} v(\sigma)\mathrm{d}s}{\int_s^{s+\delta s} v_o(\sigma)\mathrm{d}s} - 1 \\ &= \lim_{\delta s\to 0} \frac{\frac{\int_s^{s+\delta s} v(\sigma)\mathrm{d}s}{\delta s}}{\frac{\int_s^{s+\delta s} v_o(\sigma)\mathrm{d}s}{\delta s}} - 1 \\ &= \frac{v(s)}{v_o(s)} - 1 \\ &= \sqrt{\frac{[1 - r\kappa\cos((\omega-\tau)s + \psi)]^2 + (r\omega)^2}{1 + (r\omega_o)^2}} - 1, \end{aligned} \tag{6}$$

and by substituting $s = 0$ into (6), we obtain a formula that offers the strain at any certain point on the superhelix wherever the phase angle ψ is known.

$$\epsilon = \sqrt{\frac{(1 - r\kappa\cos\psi)^2 + (r\omega)^2}{1 + (r\omega_o)^2}} - 1. \tag{7}$$

Note that (7) has no τ in it, meaning that the local surface strain on the bending cylinder is independent of the torsion of the central curve, the rate of change of the bending direction of the cylinder. This is fairly counter-intuitive to us, because we know that the arc length of a superhelix largely depends on τ, as proven in our previous works [13, 14]. This also means that we cannot determine τ directly from the surface strains during the actual process of shape sensing of a cylinder, though we can of course obtain τ indirectly from its relation with ω and ψ.

2.1.1. Computing κ, ψ, and ω. Differentiating (7) with κ, ψ, and ω gives

$$\epsilon_\kappa(\kappa,\psi,\omega) = \frac{\partial\epsilon}{\partial\kappa} = -\frac{(1 - r\kappa\cos\psi)\, r\cos\psi}{\sqrt{[1 + (r\omega_o)^2]\left[(1 - r\kappa\cos\psi)^2 + (r\omega)^2\right]}}, \tag{8}$$

$$\epsilon_\psi(\kappa,\psi,\omega) = \frac{\partial\epsilon}{\partial\psi} = \frac{(1 - r\kappa\cos\psi)\, r\kappa\sin\psi}{\sqrt{[1 + (r\omega_o)^2]\left[(1 - r\kappa\cos\psi)^2 + (r\omega)^2\right]}}, \tag{9}$$

$$\epsilon_\omega(\kappa,\psi,\omega) = \frac{\partial\epsilon}{\partial\omega} = \frac{r^2\omega}{\sqrt{[1 + (r\omega_o)^2]\left[(1 - r\kappa\cos\psi)^2 + (r\omega)^2\right]}}. \tag{10}$$

At this stage, we can use the Newton–Raphson method to solve iteratively for κ, ψ, and ω to satisfy

$$\begin{aligned} \epsilon(\kappa, \psi+\theta_1, \omega) &= \epsilon_1, \\ \epsilon(\kappa, \psi+\theta_2, \omega) &= \epsilon_2, \\ \epsilon(\kappa, \psi+\theta_3, \omega) &= \epsilon_3. \end{aligned} \tag{11}$$

with the given set of strains ϵ_1, ϵ_2, and ϵ_3.

To start the iteration, suppose the values of κ, ψ, and ω are priorly given correspondingly as κ_i, ψ_i, and ω_i, i being the iteration count, and we can obtain a refined set of values by adding them to δ_κ, δ_ψ, and δ_ω. In this case, we can express

$$\begin{aligned} &\epsilon(\kappa_i,\psi_{1i},\omega_i) + [\epsilon_\kappa(\kappa_i,\psi_{1i},\omega_i)\delta_\kappa + \epsilon_\psi(\kappa_i,\psi_{1i},\omega_i)\delta_\psi + \epsilon_\omega(\kappa_i,\psi_{1i},\omega_i)\delta_\omega] = \epsilon_1, \\ &\epsilon(\kappa_i,\psi_{2i},\omega_i) + [\epsilon_\kappa(\kappa_i,\psi_{2i},\omega_i)\delta_\kappa + \epsilon_\psi(\kappa_i,\psi_{2i},\omega_i)\delta_\psi + \epsilon_\omega(\kappa_i,\psi_{2i},\omega_i)\delta_\omega] = \epsilon_2, \\ &\epsilon(\kappa_i,\psi_{3i},\omega_i) + [\epsilon_\kappa(\kappa_i,\psi_{3i},\omega_i)\delta_\kappa + \epsilon_\psi(\kappa_i,\psi_{3i},\omega_i)\delta_\psi + \epsilon_\omega(\kappa_i,\psi_{3i},\omega_i)\delta_\omega] = \epsilon_3, \end{aligned} \tag{12}$$

where $\psi_{1i} = \psi_i + \theta_1$, $\psi_{2i} = \psi_i + \theta_2$, and $\psi_{3i} = \psi_i + \theta_3$. Rewriting (12) in matrix form allows us to solve the equation for δ_κ, δ_ψ, and δ_ω quite easily by multiplying the inverse matrix on both sides.

$$\begin{bmatrix} \epsilon_\kappa(\kappa_i,\psi_{1i},\omega_i) & \epsilon_\psi(\kappa_i,\psi_{1i},\omega_i) & \epsilon_\omega(\kappa_i,\psi_{1i},\omega_i) \\ \epsilon_\kappa(\kappa_i,\psi_{2i},\omega_i) & \epsilon_\psi(\kappa_i,\psi_{2i},\omega_i) & \epsilon_\omega(\kappa_i,\psi_{2i},\omega_i) \\ \epsilon_\kappa(\kappa_i,\psi_{3i},\omega_i) & \epsilon_\psi(\kappa_i,\psi_{3i},\omega_i) & \epsilon_\omega(\kappa_i,\psi_{3i},\omega_i) \end{bmatrix} \begin{bmatrix} \delta_\kappa \\ \delta_\psi \\ \delta_\omega \end{bmatrix} = \begin{bmatrix} \epsilon_1 - \epsilon(\kappa_i,\psi_{1i},\omega_i) \\ \epsilon_2 - \epsilon(\kappa_i,\psi_{2i},\omega_i) \\ \epsilon_3 - \epsilon(\kappa_i,\psi_{3i},\omega_i) \end{bmatrix} \tag{13}$$

We then update κ, ψ, and ω correspondingly as $\kappa_{i+1} = \kappa_i + \delta_\kappa$, $\psi_{i+1} = \psi_i + \delta_\psi$, and $\omega_{i+1} = \omega_i + \delta_\omega$ to repeat the iteration until δ_κ, δ_ψ, and δ_ω all fall under the threshold.

It may be worthwhile to note that the initial values of κ_0, ψ_0, and ω_0 should be carefully chosen, as otherwise the Newton–Raphson iteration can fail to converge. It is crucial to avoid letting $\kappa_0 = 0$ or $\psi_0 = 0$, given that should either occur, ϵ_κ and ϵ_ψ become zero. Moreover, the curvature of a space curve is always non-negative by definition, implying a benefit when initializing κ_0 as a positive value. In our simulation we let $\kappa_0 = 0.01$, $\psi_0 = \frac{\pi}{2}$, and $\omega_0 = \omega_o$.

2.1.2. Computing τ. We are to determine τ from its relationship with ψ and ω;

$$\tau = \omega - \frac{\mathrm{d}\psi}{\mathrm{d}s} \tag{14}$$

Before we go further into computing τ, we initially must smooth out the values of ψ calculated for each segment in our previous step. Because (7) is periodic with respect to ψ, it is possible that the ψ values were obtained from a completely random range of angles, but it is most likely that they exist within $[-2\pi, 2\pi]$ at this point. However, for instance, from the definition of ψ, there is virtually no difference between $\psi = -2\pi$ and $\psi = 2\pi$; hence, if the ψ values of two neighboring segments are -1.999π and 1.999π, it would then be more natural to say that the difference in ψ between these two segments is 0.002π rather than 3.998π. Thus, we cannot compute $\frac{\mathrm{d}\psi}{\mathrm{d}s}$ properly with all our ψ values held within $[2-\pi, 2\pi]$, which is why we should utilize a special algorithm to smooth out ψ. We define the following for $k = 1 : N_{\mathrm{seg}}$

$$a_k = \psi_{k+1} - \psi_k - \frac{\omega_k + \omega_{k+1}}{2}\Delta s, \tag{15}$$

$$q_k = \left\lfloor \frac{a_k}{2\pi} \right\rceil, \tag{16}$$

$$m_k = a_k \pmod{2\pi}. \tag{17}$$

What we seek here is to keep every a_k within the range of $[-\pi, \pi]$. This can be achieved by executing the following algorithm:

1: **for** $k = 1$ to $N_s - 1$ **do**
2: **if** $|a_k| > \pi$ **then**
3: **if** $m_k \leqslant \pi$ **then**
4: $\psi_{(k+1):N_s} \leftarrow \psi_{(k+1):N_s} - 2\pi q_k$
5: **else**
6: $\psi_{(k+1):N_s} \leftarrow \psi_{(k+1):N_s} - 2\pi(q_k + 1)$
7: **end if**
8: **end if**
9: **end for**

Next, we should determine $\frac{\mathrm{d}\psi}{\mathrm{d}s}$ at the midpoints of the segments using the ψ values given at the midpoints of the segment. There are a number of ways by which to accomplish this, but in this study we use the ordinary cubic spline interpolation, which can be done easily with some simple MATLAB commands. Suppose `smid` is the array of parameter s at the midpoints of the segments, and `psi` is the array of ψ values of the segments. Then, we can obtain the array of $\frac{\mathrm{d}\psi}{\mathrm{d}s}$ at the midpoints as `dpsids = ppval(fnder(spline(smid, psi),1),smid)`, and we can finally determine τ by substituting these $\frac{\mathrm{d}\psi}{\mathrm{d}s}$ values in (14).

2.2. Determining the node positions from the local deformation factors.

At this stage, we calculate the overall shape of the cylinder by positioning the nodes of the central curve and the fibers. Before continuing, it may be beneficial to conduct a simple smoothing operation of our deformation variables. Here, we simply slice each cylinder segment into a number of subsegments, onto which we interpolate the deformation variables using the conventional cubic spline. This process is optional, but is found significantly to improve the accuracy of the estimation.

After smoothing, the number of segments N_{seg} is replaced with the number of subsegments $N_{\mathrm{sub}} = aN_{\mathrm{seg}}$, where a is the number of subsegments per segment. Likewise, the segment length Δs is replaced by the subsegment length $\Delta s_{\mathrm{sub}} = \frac{L}{N_{\mathrm{sub}}} = \frac{\Delta s}{a}$. The variables κ, τ and ω are defined within the segments, and thus must be splined from the midpoints of the segments, $s = \frac{(n-0.5)L}{N_{\mathrm{seg}}}$, $n = 1 : N_s$, to the midpoints of the subsegments, $s = \frac{(n-0.5)L}{aN_{\mathrm{seg}}}$, $n = 1 : aN_{\mathrm{seg}}$. In the latter process, we will need the values of ψ at the subnodes, $s = \frac{nL}{aN_{\mathrm{seg}}}$, $n = 0 : aN_{\mathrm{seg}}$; therefore it would be wise to compute these values beforehand as well.

2.2.1. Positioning the central curve and the fibers. The positions of the central nodes are determined by the Helical Extension Method (HEM), which was introduced with its efficiency proven in our previous work [15].

From our initial assumption that the cylinder is clamped at $s = 0$, the center $\mathbf{C}(0) = [0\ 0\ 0]^{\mathsf{T}}$ and the tangent $\hat{\mathbf{t}}(0) = [0\,0\,1]^{\mathsf{T}}$ are naturally given. Moreover, using ϕ at $s = 0$ as computed by cubic spline interpolation, we can easily obtain the initial normal vector $\hat{\mathbf{n}}(0)$ and binormal vector $\hat{\mathbf{b}}(0)$ as follows:

$$\begin{aligned}\hat{\mathbf{n}}(0) &= [\ \cos(-\psi)\ \ \sin(-\psi)\ \ 0\ ]^{\mathsf{T}} \\ &= [\ \cos\psi\ \ -\sin\psi\ \ 0\ ]^{\mathsf{T}},\end{aligned} \tag{18}$$

$$\begin{aligned}\hat{\mathbf{b}}(0) &= [\ \cos(-\psi + \tfrac{\pi}{4})\ \ \sin(-\psi + \tfrac{\pi}{4})\ \ 0\ ]^{\mathsf{T}} \\ &= [\ \sin\psi\ \ \cos\psi\ \ 0\ ]^{\mathsf{T}},\end{aligned} \tag{19}$$

by rotating $[1\,0\,0]^{\mathsf{T}}$ about $\hat{\mathbf{t}}(0)$ by $-\psi$ and $-\psi + \frac{\pi}{4}$, respectively. Henceforth, $\mathbf{C}(0)$ will be our $\mathbf{C}_0$, and the set of $\hat{\mathbf{t}}(0)$, $\hat{\mathbf{n}}(0)$, and $\hat{\mathbf{b}}(0)$ will form our initial TNB frame, $\hat{\mathbf{t}}_0$, $\hat{\mathbf{n}}_0$, and $\hat{\mathbf{b}}_0$, with which to start the HEM.

Subsequently, we use κ_k and τ_k for all instances of kth subsegments for $k = 1 : N_{\mathrm{sub}}$, for determination of the central node position $\mathbf{C}_k$. We determine the radius R, the elevational rate H, and the rotational rate Ω of the helix of which each of the central curve subsegments is presumed to have taken as its form, as

$$R = \frac{\kappa_k}{\kappa_k^2 + \tau_k^2}, \tag{20}$$

$$H = \frac{\tau_k}{\sqrt{\kappa_k^2 + \tau_k^2}}, \tag{21}$$

$$\Omega = \sqrt{\kappa_k^2 + \tau_k^2}. \tag{22}$$

We employ them to update the TNB frame, by rotating it with respect to the axis of the helix

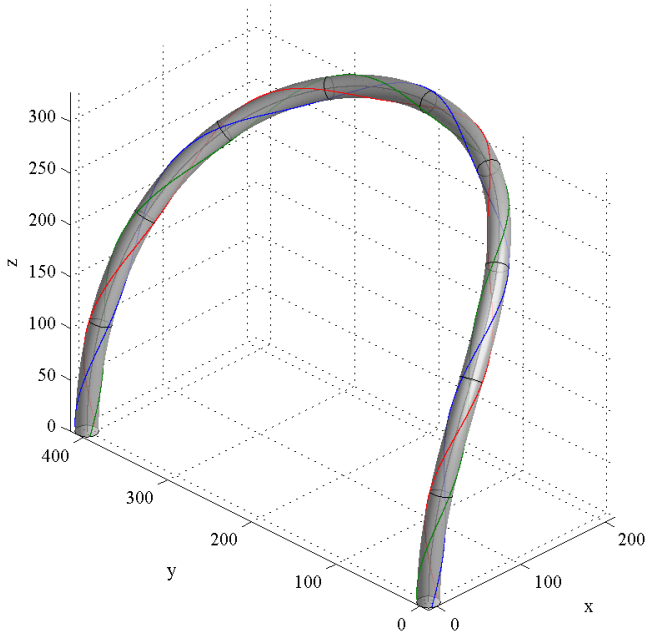

Figure 3. Example of cylinder deformation as used in our simulation. The central line was deflected into a curve that we formulated as (29), and the fibers were located by assigning ψ a value determined by (38).

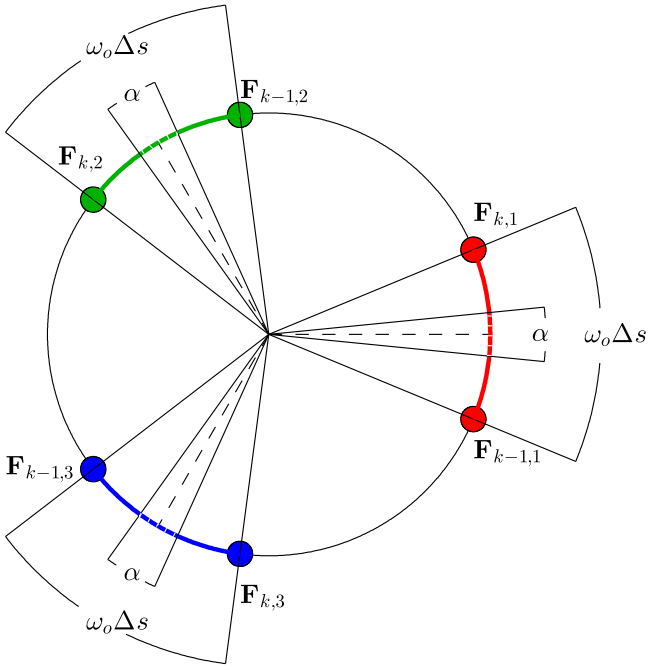

Figure 4. The rotational angle of the strain sensing region, α, was found as one of the most critical factors that affect the accuracy of shape sensing results.

$$\hat{\mathbf{w}}_k = H\hat{\mathbf{t}}_{k-1} + R\Omega\hat{\mathbf{b}}_{k-1}. \tag{23}$$

by the angle of $\gamma = \Omega\frac{\Delta s}{a}$. From Rodrigues' rotation formula,

$$\hat{\mathbf{t}}_k = \mathbf{R}\hat{\mathbf{t}}_{k-1},\ \hat{\mathbf{n}}_k = \mathbf{R}\hat{\mathbf{n}}_{k-1},\ \hat{\mathbf{b}}_k = \mathbf{R}\hat{\mathbf{b}}_{k-1}, \tag{24}$$

where $\mathbf{R}$ is the rotation matrix

$$\mathbf{R} = \begin{bmatrix} X + w_1^2(1-X) & w_1w_2(1-X) - w_3Y & w_3w_1(1-X) + w_2Y \\ w_1w_2(1-X) + w_3Y & X + w_2^2(1-X) & w_2w_3(1-X) - w_1Y \\ w_3w_1(1-X) - w_2Y & w_2w_3(1-X) + w_1Y & X + w_3^2(1-X) \end{bmatrix}, \tag{25}$$

and where $X = \cos\gamma$ and $Y = \sin\gamma$. The position of the central subnode can then be updated as

$$\mathbf{C}_k = \mathbf{C}_{k-1} + R\hat{\mathbf{n}}_{k-1} + H\Delta s\hat{\mathbf{w}}_k - R\hat{\mathbf{n}}_k. \tag{26}$$

Finally, the position of the fiber subnodes can easily be found using the $\mathbf{C}_k$ and the ψ values that we precomputed for the subnodes. We can express the direction that points toward the fiber subnodes from the central subnode as the following unit vector

$$\hat{\mathbf{f}}_{k,i} = \cos(\psi_k + \theta_i)\,\hat{\mathbf{n}}_k + \sin(\psi_k + \theta_i)\,\hat{\mathbf{b}}_k,\ i = 1,2,3. \tag{27}$$

With this, we can locate the fiber subnodes at

$$\mathbf{F}_{k,i} = \mathbf{C}_k + r\hat{\mathbf{f}}_{k,i},\ i = 1,2,3. \tag{28}$$

3. Numerical simulation

In the previous section, we demonstrated a method for the shape sensing of a cylinder using strains measured with sensors that are bound to the cylinder in triple helices. To validate our method, we conducted a simple numerical simulation with an example of a cylinder that undergoes bending and twisting deformation. We measured the strain of the fibers that are attached to the surface of the cylinder in triple helices, and used the methods we proposed in the previous sections to estimate the positions of the central nodes and the fiber nodes. We evaluated the accuracy of the results according to the position errors at the tip of the cylinder.

3.1. Undeformed cylinder

The undeformed cylinder with a radius r and length L has three strands of strain-sensing fibers bound on its surface in a triple helix configuration of a constant rate ω_o. The cylinder is clamped at $s = 0$, where the center is fixed at the origin, the longitudinal direction is the z-axis, and all three fibers are away from the origin by distance r and are pointing at angle $\theta_i = \frac{2(i-1)}{3}\pi$ for $i = 1, 2$, and 3. Thus, we can formulate the positions of the fibers on the undeformed cylinder as $\mathbf{F}_i(s) = [\cos(\omega_o s + \theta_i),\ \sin(\omega_o s + \theta_i),\ s]^{\mathsf{T}}$, $i = 1, 2$, and 3; hence, the positions of the fiber nodes can be assigned by substituting $s = 0, \Delta s, 2\Delta s, \cdots, L$, accordingly.

Because our simulation includes the process of strain measurement, we also need to position some of the points between the fiber nodes. Thus, we re-divided the entire cylinder into N_{sub} subsegments by positioning uniformly spaced $N_{\text{sub}} + 1$ subnodes all along the entire length of the cylinder in order to measure the fiber strains using the distances between them. Hence, each segment comes to have $m = N_{\text{sub}}/N_{\text{seg}}$ subsegments. Here we choose $N_{\text{sub}} = 10\,800 = 2^4 \times 3^3 \times 5^2$, which is a moderately large number with many divisors, such we can perform our numerical test with as many cases of N_{seg}s as desired. Later, we reused the same number of subsegments

in the process of shape reconstruction as well, simply for convenience.

3.2. Deformed cylinder and strain measurement

We devised an example case of a deformed cylinder that satisfies our assumptions that the cylinder is clamped at $s = 0$ and that its cross-sections remain undeformed and perpendicular. Figure 3 illustrates the overall shape of the deformation example we used.

The bending deformation is represented by the central curve, which is the curve followed by the centers of the cross sections. We made the central curve deflect into a 3D space curve that we termed a Jinguer [15]. A Jinguer is a semicircle that is drawn on a cylindrical surface, making an appropriate example for our simulation, as it is a unit-speed curve and it has smoothly varying curvature and torsion. The parametric equation of a Jinguer of length L can be written as

$$\mathbf{C}(s) = \frac{2L}{\pi^2}\begin{bmatrix} \cos\left(\frac{\pi}{2}\cos\frac{\pi s}{L}\right) \\ 1-\sin\left(\frac{\pi}{2}\cos\frac{\pi s}{L}\right) \\ \frac{\pi}{2}\sin\frac{\pi s}{L} \end{bmatrix}, \tag{29}$$

and its TNB frame is derived as

$$\hat{\mathbf{t}}(s) = \begin{bmatrix} \sin\left(\frac{\pi}{2}\cos\frac{\pi s}{L}\right)\sin\frac{\pi s}{L} \\ \cos\left(\frac{\pi}{2}\cos\frac{\pi s}{L}\right)\sin\frac{\pi s}{L} \\ \cos\frac{\pi s}{L} \end{bmatrix}, \tag{30}$$

$$\hat{\mathbf{n}}(s) = \begin{bmatrix} \frac{2\cos\frac{\pi s}{L}\sin\left(\frac{\pi}{2}\cos\frac{\pi s}{L}\right)-\pi\sin^2\frac{\pi s}{L}\cos\left(\frac{\pi}{2}\cos\frac{\pi s}{L}\right)}{\sqrt{\frac{\pi^2}{4}\left(\cos\frac{2\pi s}{L}-1\right)^2+4}} \\ \frac{2\cos\frac{\pi s}{L}\cos\left(\frac{\pi}{2}\cos\frac{\pi s}{L}\right)+\pi\sin^2\frac{\pi s}{L}\sin\left(\frac{\pi}{2}\cos\frac{\pi s}{L}\right)}{\sqrt{\frac{\pi^2}{4}\left(\cos\frac{2\pi s}{L}-1\right)^2+4}} \\ -\frac{2\sin\frac{\pi s}{L}}{\sqrt{\pi^2\sin^4\frac{\pi s}{L}+4}} \end{bmatrix}, \tag{31}$$

$$\hat{\mathbf{b}}(s) = \begin{bmatrix} -\frac{2\sin^2\frac{\pi s}{L}\cos\left(\frac{\pi}{2}\cos\frac{\pi s}{L}\right)}{\sqrt{\pi^2\sin^4\frac{\pi s}{L}+4}} - \frac{\cos\frac{\pi s}{L}\left[2\cos\frac{\pi s}{L}\cos\left(\frac{\pi}{2}\cos\frac{\pi s}{L}\right)+\pi\sin^2\frac{\pi s}{L}\sin\left(\frac{\pi}{2}\cos\frac{\pi s}{L}\right)\right]}{\sqrt{\frac{\pi^2}{4}\left(\cos\frac{2\pi s}{L}-1\right)^2+4}} \\ \frac{2\sin^2\frac{\pi s}{L}\sin\left(\frac{\pi}{2}\cos\frac{\pi s}{L}\right)}{\sqrt{\pi^2\sin^4\frac{\pi s}{L}+4}} + \frac{\cos\frac{\pi s}{L}\left[2\cos\frac{\pi s}{L}\sin\left(\frac{\pi}{2}\cos\frac{\pi s}{L}\right)-\pi\sin^2\frac{\pi s}{L}\cos\left(\frac{\pi}{2}\cos\frac{\pi s}{L}\right)\right]}{\sqrt{\frac{\pi^2}{4}\left(\cos\frac{2\pi s}{L}-1\right)^2+4}} \\ \frac{\pi\sin^3\frac{\pi s}{L}}{\sqrt{\pi^2\sin^4\frac{\pi s}{L}+4}} \end{bmatrix}. \tag{32}$$

From this TNB frame, the curvature and torsion are given as

$$\kappa(s) = \frac{\pi}{4L}\sqrt{\pi^2\left(\cos\frac{2\pi s}{L}-1\right)^2+16}, \tag{33}$$

and

$$\tau(s) = \frac{\pi^2\sin\frac{2\pi s}{L}}{4L}\left(\frac{32}{\pi^2\left(\cos\frac{2\pi s}{L}-1\right)^2+16}+1\right). \tag{34}$$

The position of the fibers after deformation can be prescribed by determining ψ as a function of s. It follows from (14) that

$$\psi(s) = \int_0^s [\omega(\sigma)-\tau(\sigma)]\,\mathrm{d}\sigma, \tag{35}$$

which, when substituted with (34), gives us

$$\psi(s) = \int_0^s \omega(\sigma)\mathrm{d}\sigma - \tan^{-1}\left[\frac{\pi}{2}\sin^2\frac{\pi s}{L}\right] - \frac{\pi}{4}\sin^2\frac{\pi s}{L}. \tag{36}$$

In our simulation we assigned a slight perturbation to the rotational rate of the fibers, as follows

$$\omega(s) = \omega_o + \alpha\sin\frac{2\pi s}{L}, \tag{37}$$

which gives us

$$\psi(s) = \omega_o s - \frac{\alpha L}{2\pi}\cos\frac{2\pi s}{L} - \tan^{-1}\left[\frac{\pi}{2}\sin^2\frac{\pi s}{L}\right] - \frac{\pi}{4}\sin^2\frac{\pi s}{L}. \tag{38}$$

The fiber positions can then be assigned by the formulae (27) and (28), where the normal and binormal vectors are given by (31) and (32), respectively.

Although the strain is originally defined as a function of the position directly at the sampling point, most practical strain-sensing techniques include a process by which they obtain the average value of the strains within a certain region around the sampling point. In order to mimic such a process, we evaluated the strain using a certain number of subsegments that are adjacent to the fiber segment's midpoint. The strain is obtained from the change in the length of the strain sensing region, which is approximated by the sum of the distances between consecutive subnodes. The number of subsegments chosen in this procedure is an even positive integer, μ. Since each segment is divided into m subsegments, the length of the strain sensing region before deformation can be represented as $\frac{\mu}{m}\Delta s$. Expressly, for $k = 1, \cdots, N_{\text{seg}}$ and $i = 1, 2$, and 3, we computed the strain of the ith fiber in the kth segment as

$$\epsilon_{k,i} = \frac{\sum_{n=(k-\frac{1}{2})m-\frac{1}{2}\mu}^{(k-\frac{1}{2})m+\frac{1}{2}\mu-1}\sqrt{[\tilde{x}_{n+1,i}-\tilde{x}_{n,i}]^2+[\tilde{y}_{n+1,i}-\tilde{y}_{n,i}]^2+[\tilde{z}_{n+1,i}-\tilde{z}_{n,i}]^2}}{\sum_{n=(k-\frac{1}{2})m-\frac{1}{2}\mu}^{(k-\frac{1}{2})m+\frac{1}{2}\mu-1}\sqrt{[\bar{x}_{n+1,i}-\bar{x}_{n,i}]^2+[\bar{y}_{n+1,i}-\bar{y}_{n,i}]^2+[\bar{z}_{n+1,i}-\bar{z}_{n,i}]^2}} - 1, \tag{39}$$

where $\tilde{x}, \tilde{y}$, and $\tilde{z}$ denotes the coordinates in the global frame of the fiber subnodes after deformation, and $\bar{x}, \bar{y}$, and $\bar{z}$ before deformation. We used these strains as the inputs to locate the

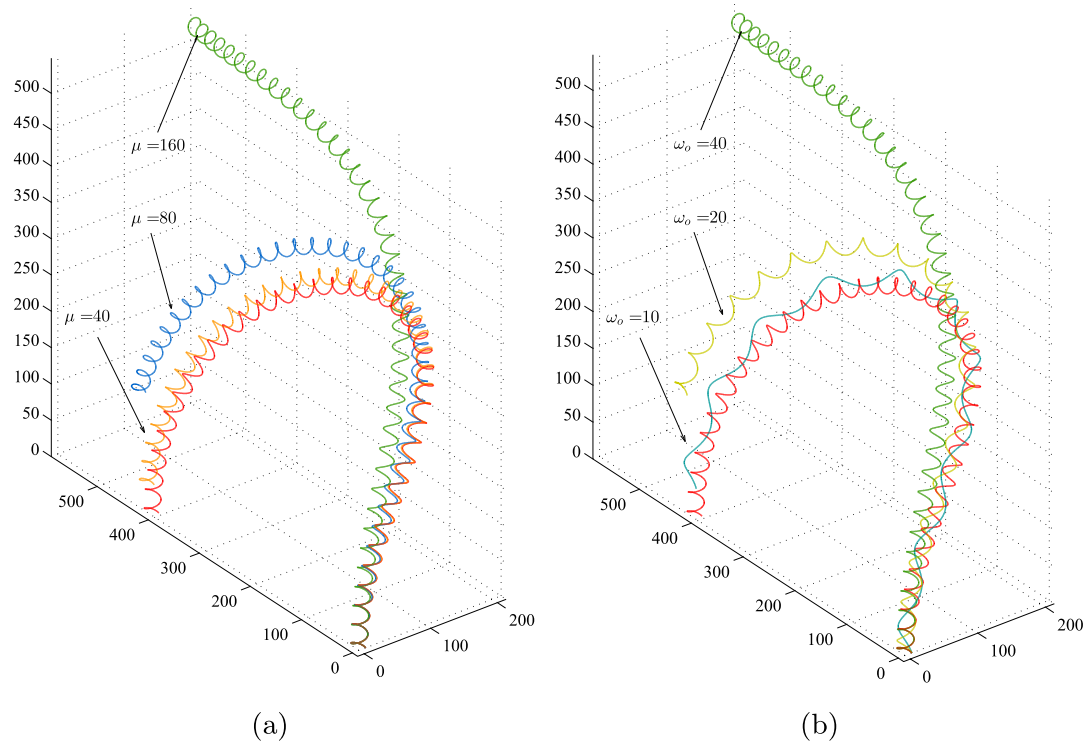

Figure 5. The estimated shape of the first fiber $\mathbf{F}_1(s)$ with (a) $N_{\text{seg}} = 10$; $\omega_o = 40$ rev/L; and $\mu = 40, 80$, and 160, and (b) $N_{\text{seg}} = 10$; $\mu = 160$; and $\omega_o = 10, 20$, and 40 rev/L. The total number of subsegments was $N_{\text{sub}} = 10\,800$ for both (a) and (b). The true fiber shape is presented as red curves, and in (b) it is only shown for the case of $\omega_o = 40$ for convenience.

central and fibral subnodes, following the procedure covered in section 2.

3.3. Results

We conducted our numerical tests for various cases, each case with differing values of N_{seg}, ω_o, m, μ, and r, and we collected the estimated positions to evaluate the accuracy. It took from 2.5 to 3 s of time to purely determine the shape from the given strains for each case in MATLAB, hence the proposed method would be applicable to real-time shape sensing by adopting a faster computational tool. The calculation time depended much more strongly on N_{sub} than on N_{seg}, which means most of the computation was carried out on reconstructing the shape from the smoothed local deformation factors.

Since our method is bound to have some spatial drift error along the arc length, the error is predictably greatest at the end of the cylinder. Hence, we chose to evaluate the accuracy by comparing the true and the estimated positions of the tip of the red fiber, namely, $\mathbf{F}_{N_{\text{sub}},1}$.

It was observed from our simulation results that the accuracy of the estimation largely depend on two major factors: α, which is the rotational angle of the sensing region of the fiber with respect to the central axis of the cylinder, and δ, which is the length of a segment divided by the length of the entire cylinder and hence is the reciprocal of N_{seg}. The angle that α represents within a segment is as illustrated in figure 4. Thus with the given values of L, m, μ, and ω_o, we can determine α as

$$\alpha = \frac{\mu\omega_o L}{m}. \tag{40}$$

A trend towards growth in the errors was observed with larger values of α and δ, and the error was found to depend more strongly on α than on δ. Generally, the influence of δ was noticeable only when both α and δ were very small, while otherwise α appeared much more dominant. For relatively larger values of α, the effect of δ appeared to be mostly insignificant.

Figures 5(a) and (b) presents the correspondence between α and the position error of the red fiber node at $s = L$. We fixed all other variables but varied only ω_o and μ, for (a) and (b), respectively, such that both plots contained the same values of α. We can clearly observe, even with differing values of ω_o and μ, that if we have the same value of α, the result will be then similar in terms of accuracy.

We speculate the reason for this α-dependence of the accuracy as follows. Since we assume that the strain is measured right at the midpoint of each fiber segment, it is quite natural to expect a better estimation when the actual measurement is focused better at the midpoints. The dependence could also be on the length, instead of the rotational angle, of the region, but considering how the surface strain of a deforming rod varies with the angle from the bending direction, we may find the dominance of α to be relatively intelligible, unless the rate of change of the bending direction is much faster than the rotational rate of the fibers.

Figure 6 shows the position errors collected from the results of various cases with differing values of

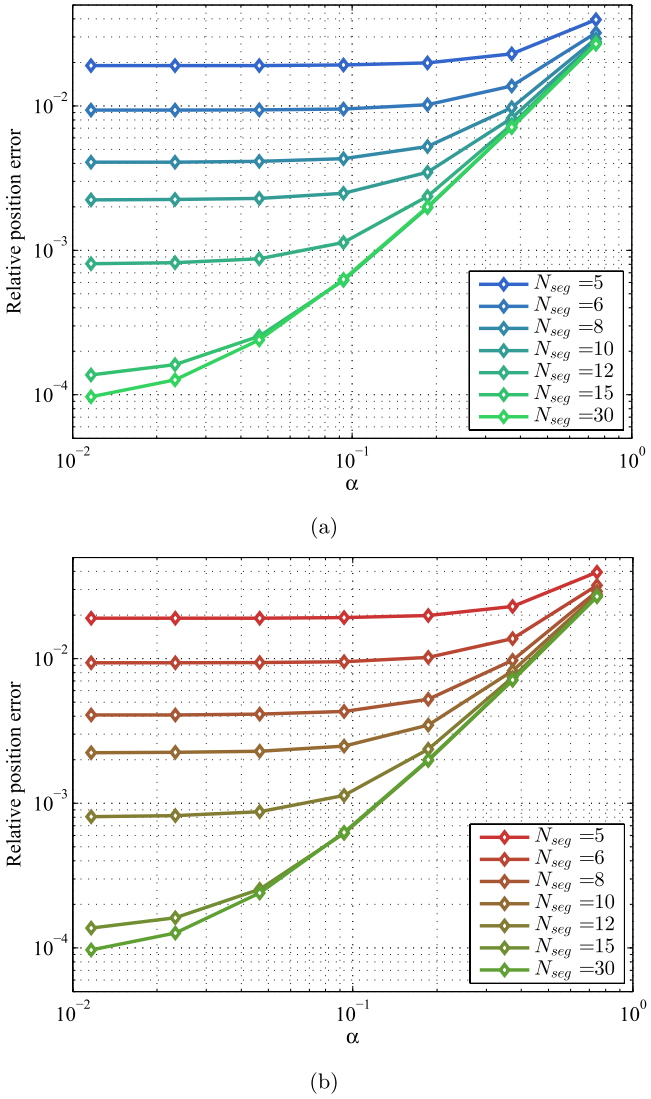

Figure 6. Position errors with $N_{\text{seg}} = 5, 6, 8, 10, 12, 15, 30$, with the remaining instances given as (a) $\omega_o = 5$, and $\mu = 4, 8, 16, 32, 64, 128, 256$, and (b) $\omega_o = 5, 10, 20, 40, 80, 160, 320$, and $\mu = 4$. The values of ω_o and μ were selected such that α took the same set of values across the two subfigures.

$N_{\text{seg}} = 5, 6, 8, 10, 12, 15,$ and 30; $\omega_o = 5, 10, 20, 40, 80, 160,$ and 320; and $\mu = 4, 8, 16, 32, 64, 128,$ and 256. Here, we fixed and varied the values of ω_o and μ alternatively, as we did in figure 5, such that the two subplots can contain the same set of values of α, which in turn caused the results they show to be of a striking similarity. We can observe here the qualitative trend referred to above; specifically, the dependence on δ becomes stronger with a lower α and a higher δ, and weaker with a higher α and a lower δ. In order to investigate this tendency in more depth, we also tested the following cases: $N_{\text{seg}} = 5, 6, 8, 9, 10, 12, 15, 18, 20, 24,$ and 30; $\omega_o = 5, 10, 15, 20, 25,$ and 30; and $\mu = 4, 8, 16,$ and 32. We used MATLAB's surface fitting tool in order to analyze the overall tendency of convergence, finding that the effect of α and δ on the position error can be approximated as

$$E = 0.9011\mathrm{e}^{5.113\alpha} + 0.4453\mathrm{e}^{18.88\delta} - 2.089. \qquad (41)$$

Of course, (41) is only a result of an approximate fitting that is specialized for one specific deformation example as used in the simulation here; hence, we can scarcely consider it as a general relation. However, this at least provides a tentative glimpse of how α and δ are roughly related to the accuracy of our method. Further studies on this subject would be useful.

4. Conclusion

In summary, we have demonstrated a numerical method by which to estimate the deformation state of a cylinder using data received from a set of strain sensors attached to the surface of the cylinder in a triple helix configuration. The method is a two-stage process. First, we determine the local deformation factors from the strains, after which we determine the overall shape using the deformation factors.

The local deformational rates are computed from the surface strains by Newton–Raphson iteration with an analytical strain formula. This strain formula is based on our original superhelix model, which precisely describes the strain on the surface of a cylinder under bending and twist deformation. The positions of the centers of the cross-sections are computed by the Helical Extension Method, of which the accuracy and efficiency were verified in our previous work. The positions of the fibers are obtained from the normal and binormal vectors of the central curve.

We validated our method in a simulation with a virtual cylinder that is deformed into an analytically prescribed shape. The simulation was conducted with various numbers of measuring segments and various initial rates of spin. The results showed that the proposed method can estimate the shape of a deformed cylinder with remarkable precision. It was observed that the accuracy of estimating the shape depends on two quantities: α, the rotational angle of the measuring region of each segment, and δ, the length of a segment divided by the length of the entire cylinder. It appeared from data fitting that position errors are approximated in the form of an exponential surface of (41).

In order to alleviate this problem of α-dependence, it may be worthwhile to re-adopt the formula for the arc length of a superhelix from our previous works [13, 14]. In our preliminary tests, where we modeled the changed length of the strain-sensing interval as the arc length of a segment of a superhelix, it was observed that the influence of α on the accuracy was dramatically reduced. However, given that the arc length formula itself is very long and complicated, the computation process can become excessively heavy. Hence, assessing the fiber strain at the midpoint of each segment, as is done here, appears to be the most efficient and elegant method we have for now. Further studies will be required to refine the arc length formula and modify the computational process of shape estimation accordingly.

We can also interpret our simulation results from the perspective of sensor design. Currently, there exist a small number of multicore fiber products whose cores are spun into helices so they can work as 3D shape sensors. These products are usually spun at relatively high rates; for example, Fibercore's SSM-7C1500 has a spin pitch of the cores of approximately 1.53 centimeters. If one is to use this fiber as a shape sensor, the spatial resolution used during the strain measurement should be 2.4 millimeters or less to keep α less than one radian. Despite all of the various types of optical strain-sensing methods, there are not many methods other than OFDR that can provide a spatial resolution this high. Furukawa's multicore fiber with continuous Bragg gratings, employed by Westbrook *et al* (2017) [12], has a spin pitch of 2 centimeters and provides spatial resolution up to 40 microns by the use of OFDR, and hence makes $\alpha = 0.0126$ radians. This is actually small enough to keep the relative position error at the end node less than 10^{-4} by our proposed method, provided that the strains are precisely measured. However, we can generally state that a spun multicore fiber would work more effectively and more versatilely as a shape sensor if it were spun at a much lower rate.

This study provides a basis for subsequent studies of optical shape sensing by founding a concise and reliable numerical method. Most notably, this is the first study to our knowledge to investigate the effect of the initial rate of spin of the sensor array on the accuracy of the result. Our future efforts will focus on applying this numerical method in a laboratory experiment.

Acknowledgments

This research was supported by the Climate Change Research Hub of KAIST (Grant No. N11160021), the Korea Institute of Energy Technology Evaluation and Planning (KETEP), the Ministry of Trade, Industry & Energy (MOTIE) of the Republic of Korea (No. 20168520021200), and the Industrial Core Technology Development Program (Project ID: 10063452) funded by the Ministry of Trade, Industry and Energy of the Korean government. The authors gratefully acknowledge their support.

ORCID iDs

Sungyeop Lim https://orcid.org/0000-0001-9515-9417

References

[1] Wilk L S 1988 Strain measurement apparatus and method *US Patent* no. 4,788,868 A
[2] Zhang Y N, Liu Z, Shen L Y and Qian J W 2013 Detection of pipeline curvature with FBG sensors twisted *Appl. Mech. Mater.* **303–6** 67–73
[3] Zhang L, Qian J, Zhang Y and Shen L 2005 On SDM/WDM FBG sensor net for shape detection of endoscope *Proc. IEEE Int. Conf. on Robotics and Automation* pp 1986–91
[4] Yi X, Qian J, Zhang Y, Zhang Z and Shen L 2007 3D shape display of intelligent colonoscope based on FBG sensor array and binocular vision *IEEE/ICME Int. Conf. on Complex Medical Engineering* pp 14–9
[5] Park Y-L, Elayaperumal S, Daniel B, Ryu S C, Shin M, Savall J, Black R J, Moslehi B and Cutkosky M R 2010 Real-time estimation of three-dimensional needle shape and deflection for MRI-guided interventions *IEEE/ASME Trans. Mechatronics* **15** 906–15
[6] Pauer H, Ledermann C, Weede O and Woern H 2013 Towards building a miniaturized shape sensor: building process of a shape sensor for use in single port surgery *7th Int. Conf. on Sensing Technology* pp 549–54
[7] Moon H, Jeong J, Kang S, Kim K, Song Y-W and Kim J 2014 Fiber-Bragg-Grating-Based ultrathin shape sensors displaying single-channel sweeping for minimally invasive surgery *Opt. Lasers Eng.* **59** 50–5
[8] Askins C G, Miller G A and Friebele E J 2008 Bend and twist sensing in a multiple-core optical fiber *Conf. on Optical Fiber Communication/National Fiber Optic Engineers Conf.* (https://doi.org/10.1109/OFC.2008.4528404)
[9] Moore J P and Rogge M D 2012 Shape sensing using multi-core fiber optic cable and parametric curve solutions *Opt. Express* **20** 2967–73
[10] Froggatt M E, Klein J W, Gifford D K and Kreger S T 2014 Optical position and/or shape sensing *US Patent Specification* 8,773,650 B2
[11] Childers B A, Gifford D K, Duncan R G, Raum M T, Vercellino M E and Froggatt M E 2010 Fiber optic position and shape sensing device and method relating thereto *US Patent Specification* 7781724 B2
[12] Westbrook P S, Feder K S, Kremp T, Ko W, Wu H, Monberg E, Simoff D A, Bradley K and Ortiz R 2017 Distributed sensing over meter lengths using twisted multicore optical fiber with continuous Bragg gratings *Furukawa Electr. Rev.* **48** 26–32
[13] Lim S and Han S 2016 A formula for the Arc length of a superhelix *Sens. Smart Struct. Technol. Civ. Mech. Aerosp. Syst.* **9803** 980327
[14] Lim S and Han S 2018 Series representations for the rectification of a superhelix *Appl. Math. Modelling* **56** 381–8
[15] Lim S and Han S 2017 Helical extension method for solving the natural equation of a space curve *Surf. Topography: Metrol. Prop.* **5** 035002